Stacking faults in an O2-type cobalt-free lithium-rich layered oxide: mechanisms of the ion exchange reaction and lithium electrochemical (de)intercalation

Valentin Saïbi, Laurent Castro, Issei Sugiyama, Stéphanie Belin, Claude Delmas, Marie Guignard

Stacking Faults in an O2-type Cobalt-Free Lithium-Rich Layered Oxide: Mechanisms of the Ion Exchange Reaction and Lithium Electrochemical (De)Intercalation

*Valentin Saïbi[#] Laurent Castro[§], Issei Sugiyama[◊], Stéphanie Belin[•], Claude Delmas[#], Marie Guignard[#,]**

[#] University of Bordeaux, CNRS, Bordeaux INP, ICMCB, UMR 5026, 33600 Pessac, France

§ Material Engineering Division, Toyota Motor Europe NV/SA, Technical Center, 1930 Zaventem, Belgium

◊ Advanced Battery Division, Toyota Motor Corporation, Mishuku 1200, Susono-shi, Shizuoka, Japan 410-1193

• Synchrotron SOLEIL, L'Orme des Merisiers, 91190 Saint-Aubin, France

Abstract. The metastable O2-type cobalt-free lithium-rich layered oxide $Li_{0.84}Ni_{0.14}Mn_{0.72}O_2$ was successfully prepared by a new all solid-state ion-exchange reaction from the P2-type sodium layered oxide precursor $Na_{0.7}[Li_{0.14}Ni_{0.14}Mn_{0.72}]O_2$ using lithium chloride at moderate temperature. The particular oxygen stacking in the resulting O2-type structure is assumed to suppress the detrimental layer-to-spinel phase transition usually observed upon cycling in

conventional O3-type lithium-rich layered oxides due to the irreversible migration of transition metal cations, causing substantial voltage decay and capacity fading. Despite the existence of stacking faults originating from the P2-to-O2 topotactic reaction during the Na^+-to-Li^+ exchange, evidenced by X-ray diffraction simulation and high-resolution microcopy, the electrochemical tests conducted on the faulted O2-type positive electrode material revealed a greatly improved reversible (de)intercalation mechanism along with high specific capacity values. An *operando* X-ray diffraction study indicated that there are only small structural changes upon cycling and that they are stable and reversible. Moreover, *operando* X-ray absorption spectroscopy experiments showed that a large part of the capacity relies on the oxygen redox which is also reversible upon cycling.

Introduction

The main limitation to power portable devices and electric vehicles comes from the positive electrode side, for which the current available commercial materials ($LiCoO_2$, $LiFePO_4$, $LiMn_2O_4$ etc.) are suffering from low specific capacities (<180 mAh/g) and then low gravimetric (Wh/kg) and volumetric (Wh/l) densities. Therefore, the development safe and mostly high energy density cathodes (> 300 Wh/kg) is key to the implementation of large-scale rechargeable lithium-ion batteries. Apart from their electrochemical properties, the cost and the environmental impact of raw materials are increasingly taken into consideration. Although cobalt has been extensively used in lithium-ion batteries, this transition metal (TM) cation has not only become rare and consequently expensive, it is also harmful to health and the environment, and implies both political and ethical issues[1]. This element is now listed as one of the strategic raw materials defined by the European Union (EU) commission and may be subject to regulations in EU in the coming years. For those reasons, research has been dedicated to finding alternative materials to $LiCoO_2$, leading to the development of cheaper NCA (Nickel,

Cobalt, Aluminum) or Ni-rich NMC (Nickel, Manganese, Cobalt) lithium layered oxides with lower Co content, along with other new cobalt-free layered oxides.

Among the currently reported layered metal oxide positive electrode materials, lithium-rich layered oxides $Li_{1+x}M_{1-x}O_2$ (M : 3d TM cations) are promising candidates for next generation lithium-ion batteries. The larger amount of lithium ions contributes to provide higher specific capacity (> 280 mAh/g) with batteries operating at a higher voltage (>3.5V vs. Li+/Li in average) than conventional lithium layered oxides $LiMO_2$ due to the activation of the anionic redox[2-4]. The most famous and extensively studied lithium-rich layered oxide is probably $Li_{1.2}Ni_{0.13}Mn_{0.54}Co_{0.13}O_2$[5-9]. This positive electrode material can deliver a very high specific capacity of more than 300 mAh/g during the first charge, attributed not only to the TM cations $Ni^{2+/4+}$ and $Co^{3+/4+}$ redox but also to the participation of anionic oxygen redox $O^{2-/\delta-}$. However, practical applications are partly hindered by some major drawbacks including fast voltage decay and continuous capacity fading. The unstable nature of the oxidized oxide ions is responsible for detrimental structural changes upon cycling such as the irreversible layer-to-spinel phase transition originating from partial oxygen loss at high voltage. Therefore, the battery has poor cycling performances (low rate capability) and low energy efficiency (large voltage hysteresis)[10-12].

A recent study by Eum *et al.* suggests that the main cause of voltage decay at a low lithium content is not necessarily the migration of TM cations itself, but rather that the TM ions permanently occupy Li sites during the subsequent charge/discharge cycles, preventing the successful return of Li ions within the interslab[13]. The study of the migration pathway in typical O3-type lithium-rich layered oxide structure further reveals that the oxygen stacking and the TMO_6 environment are probably responsible for the easy intra-layer movements of small TM cations. Most lithium-rich layered oxides adopt an O3-type structure according to the classification proposed by Delmas *et al.*[14], where the oxide ions pack in an ABCABC sequence

with lithium ions occupying octahedral sites in the interslab space, and TMO_6 octahedra sharing edges with adjacent LiO_6 octahedra.

In contrast, in O2-type structures, the unique oxygen stacking sequence ABCBAB (or ABACAB) leads to octahedral sites for lithium sharing edges with one TMO_6 octahedron on one side, but also one face with another TMO_6 octahedron on the other side[15]. The migration of TM cations would inevitably occur but the strong electrostatic repulsions would restrict the movement of TM ions in the lithium interslab space and enhance their reversible return within their own original layers[13]. Paulsen *et al.* reported that the layered-to-spinel structural transition did no longer occur in O2-type $Li_{2/3}[Li_{1/6}Mn_{5/6}]O_2$[16]; more recently, Umeno *et al.* studied the O2-type Li-rich layered ruthenium oxide $Li_{1.22-x}Ru_{0.78}O_2$ where the Ru migration is successfully blocked owing to the nature of the O2 stacking[17].

O2-type Li-rich layered oxides are metastable and cannot be obtained by common high temperature solid-state lithiation methods (>600°C). Their synthesis requires much lower temperatures of 120-300°C that can only be achieved by soft chemistry routes. They are obtained from a sodium-based P2-type structure by the Na^+-to-Li^+ exchange thanks to the planar and local gliding of the oxygen stacking layers. During this P2-to-O2 topotactic reaction, TMO_2 layers made of edge-sharing TMO_6 octahedra glide and the sodium prismatic sites in the interslab space gradually convert into octahedral sites where lithium ions are more stabilized. Most of the ion exchange reactions have been conducted with lithium salt (LiCl and $LiNO_3$, mostly) in solvothermal conditions[13,18,19,20] or via molten salts methods[20,21,22]. On the other hand, very few paper report solid-state ion-exchange reaction[23]. Herein, we developed a new all solid-state ion-exchange reaction using little excess of lithium chloride precursor at moderate temperature to prepare the metastable O2-type cobalt-free lithium-rich layered oxide $Li_{0.84}Ni_{0.14}Mn_{0.72}O_2$ from the sodium-based analogue P2-$Na_{0.7}[Li_{0.14}Ni_{0.14}Mn_{0.72}]O_2$. The structural and electrochemical properties of the lithiated layered oxide were then studied.

Experimental Section

Syntheses. Nickel oxide NiO and manganese oxide MnO_2 precursors were both obtained from nitrates decomposition at 450°C for 15 hours under oxygen atmosphere. Sodium and lithium carbonates were dried under vacuum at 200°C for 15 hours. All chemical compounds were stored in an Ar-filled glovebox to avoid any air contamination. Sodium layered oxide P2-$Na_{0.7}[Li_{0.14}Ni_{0.14}Mn_{0.72}]O_2$ was prepared by solid state synthesis. Stoichiometric amount of Na_2CO_3 (Alfa Aesar, 99.5%) Li_2CO_3 (Aldrich, 99.99%) , NiO and MnO_2 were grinded in an agate mortar in an Ar-filled glovebox (H_2O and O_2 < 0.5 ppm) at room temperature. Sodium and lithium carbonates were introduced with a 5% and 3% excess, respectively, in order to balance alkaline evaporation during thermal treatment. The mixture was packed in a golden crucible and introduced in a tubular furnace for a one-step calcination at 850°C for 10 days under air atmosphere. This very long heat treatment time for the synthesis of the P2-type phase was chosen in order to obtain a very well crystallized O2-type phase after the ion-exchange reaction, as proposed by Paulsen *et al.*[24] After the heat treatment, the P2-$Na_{0.7}[Li_{0.14}Ni_{0.14}Mn_{0.72}]O_2$ phase was always stored in the Ar-filled glovebox.

Lithium layered oxide O2-$Li_{0.84}Ni_{0.14}Mn_{0.72}O_2$ was obtained by ion-exchange reaction from P2-$Na_{0.7}[Li_{0.14}Ni_{0.14}Mn_{0.72}]O_2$ by an all solid-state route. 250 mg of the sodium P2-phase were mixed with LiCl (Acrocs Organics, 99%) (1.5 moles of LiCl for 1 mole of P2-$Na_{0.7}[Li_{0.14}Ni_{0.14}Mn_{0.72}]O_2$) in an agate mortar in the Ar-filled glovebox at room temperature. The ion exchange was achieved by solid state reaction with LiCl rather than LiI which had been used by J. M. Tarascon[23] as a redox reaction was found to occur with LiI with the production of gaseous I_2. The mixture was shaped into a 13 mm diameter and 400 mg pellet pressed under 5 tons. The pellet was then heated at 300°C for 4 hours in a glass tube under dynamic vacuum (P < 10^{-3} mbar). Once cooled down to room temperature, the glass tube was introduced back in an Ar-filled glovebox and the pellet was ground into powder, then washed

and filtered three times with anhydrous methanol (8 mL each time). The remaining solvent was evaporated overnight at room temperature directly in the Ar-filled glovebox.

Powder X-ray diffraction. The solid-state ion-exchange reaction was monitored using variable temperature powder X-ray diffraction. The experiment was conducted in an Xpert3 diffractometer (Malvern) with an Xcelerator detector using a Co $K\alpha_1$-$K\alpha_2$ source (λ = 1.7889 Å) in the 2θ-range 16°-80° with a 0.016° step size. The mixture containing the same LiCl:P2-$Na_{0.7}[Li_{0.14}Ni_{0.14}Mn_{0.72}]O_2$ molar ratio (1.5:1) was first loaded in a alumina crucible as a powder in the Ar-filled glovebox. The alumina crucible was then quickly installed in an Anton Paar HTK 1200 oven chamber filled with helium to limit any reaction of the mixture with the atmosphere. The diffraction patterns were recorded every 25°C during 2 hours. A 5°C/min heating rate was used and a waiting time of 15 minutes was applied prior to the measurements to ensure a good homogenization of the temperature within the sample.

Phase purity was always checked using laboratory powder X-Ray Diffraction on an Xpert3 diffractometer with an Xcelerator detector using a Cu $K\alpha_1$-$K\alpha_2$ source (λ = 1.5418 Å) in the 2θ-range 10°-80° with a 0.016° step size. The samples were loaded in a glovebox in a 0.3 mm diameter borosilicate glass capillary sealed under argon. The same capillaries were used to perform Synchrotron Powder X-ray diffraction during two different beamtimes at MSPD beamline at Alba synchrotron (Spain) using the MYTHEN detector. Synchrotron X-ray diffraction pattern of P2-$Na_{0.7}[Li_{0.14}Ni_{0.14}Mn_{0.72}]O_2$ was recorded using a wavelength λ = 0.6191 Å in the 2θ-range 0°-82° with a 0.006° step size, whereas that of O2-$Li_{0.84}Ni_{0.14}Mn_{0.72}O_2$ was recorded using a wavelength λ = 0.7286 Å in the 2θ-range 0°-72° with a 0.006° step size.

Chemical analyses. Chemical compositions were confirmed by Inductively Coupled Plasma – Optical Emission Spectroscopy (ICP-OES) for elemental analysis on Na, Li, Ni and Mn using a Varian Model 720-ES spectrometer. The powders were first dissolved into a concentrated aqua regia (HCl/HNO_3) solution and then diluted with distilled water.

Morphological features of the different samples were observed on a Zeiss EVO 50 scanning electron microscope at an acceleration voltage of 15kV and on a JEOL JSM-6700 F scanning electron microscope at an acceleration voltage of 5kV. In order to avoid charging effects, a 2-nm thick layer of platinum was deposited by cathodic sputtering on the samples.

X-ray absorption spectroscopy. (XAS) was performed in transmission mode using the Si(111) double-crystal monochromator at SAMBA beamline, Soleil Synchrotron facility (France). Reference samples were diluted in boron nitride and pelletized with a mass loading calculated so that the edge jump at Mn and Ni K-edge is equal to 0.8. Pellets were packed in Ar-filled plastic bag to avoid air exposure. A Mn and Ni metal foils were used for the energy calibration of all samples. Fastosh software was used to process the spectra[25].

Electrochemical properties were measured in CR2032-type coin-cells. Positive electrodes of 15 mg and 10 mm diameter were made of active material (88 weight %), graphite/carbon black 50:50 (10 weight %) as electronic conductor and polytetrafluoroethylene (PTFE) (2 weight %) as binder, together mixed in an agate mortar in an Ar-filled glovebox at room temperature. Metallic lithium foil of 12 mm diameter and 135 µm thick was scrubbed on both sides and it was used as negative electrode. The positive and negative electrodes were separated by one Viledon and two Celgard separators. The electrolyte solution was 1M $LiPF_6$ dissolved in PC:EC:DMC (1:1:1 volume %). The assembled cells were cycled in galvanostatic mode using VMP-3 (Biologic) at a C/20 current rate (theoretical (de)intercalation of one lithium ion per formula unit in 20 hours). For *operando* X-ray diffraction experiments, the same formulation for the positive electrode was used, whereas it was optimized for *operando* X-ray Absorption spectroscopy to allow the best possible measurement conditions both at the Mn and Ni K-edges. The electrode composition was then a mixture of 65 weight % of active material, 30 weight % of graphite/carbon black 50:50 and 5 weight % of PTFE. For both o*perando* experiments, the same electrolyte, separators and lithium foil as in the coin cells were used.

Finally, specific electrochemical cells were used for these experiments: a lab-made cell was used for X-ray diffraction working in reflection mode and a Leriche-type cell was used for the X-ray absorption spectroscopy working in transmission[26]. In both cases, beryllium windows were used as current collector to allow X-ray transmission trough the cell.

Transmission electron microscopy (TEM) was performed with JEOL ARM-200F operated at 200 kV. Thin foil for TEM observation was carried out using focused ion beam (FIB) system (Hitachi X Vision) and Ar-ion milling (Gatan PIPS2). All sample preperations and observations were carried out in Ar atmosphere or in vacuum without air exposure.

Results and Discussion

Crystal structure of the sodium-based layered oxide P2-$Na_{0.7}[Li_{0.14}Ni_{0.14}Mn_{0.72}]O_2$ was studied by synchrotron X-ray diffraction. The diffraction pattern of the sodium phase can be first indexed in the conventional $P6_3/mmc$ space group, indicating the successful synthesis of the sodium-based phase. This material crystallizes with a P2-type stacking with an ABBA oxygen stacking: sodium ions occupy trigonal prismatic sites whereas Li, Ni and Mn can be found in octahedral sites in the TM layers. Additional diffraction peaks in the lower 2θ-range were also visible. They originate from the long range in-plane ordering of large Li/Ni and small Mn cations (the ionic radii for the different ions are: $r(Li^+)$ = 0.76 Å, $r(Ni^{2+})$ = 0.69 Å and $r(Mn^{4+})$ = 0.53 Å[27]) in order to minimize the structural strains as well as to optimize the charge distribution, creating a honeycomb structure in the TM layers. Those well-known superlattice diffraction peaks can be taken into account in a larger cell $a\sqrt{3} \times a\sqrt{3} \times c$.

The synchrotron X-ray diffraction pattern of the sodium phase was then indexed in the $P6_3$ space group and a Rietveld refinement of its structure was undertaken. The cell parameters and the atomic positions determined from this refinement are given in Table S1 and the calculated synchrotron X-ray diffraction pattern is in good agreement with the experimental one (Figure

1). One can however notice that the experimental intensity of the additional reflections, resulting from the in-plane TM ordering and visible in the 2θ-range 8-13°, is much lower than that calculated ones. This could come from the presence of faults in the stacking of the TM layers along the c axis. The three-dimensional description of the structure obtained from the *P*6$_3$ space group imposes a regular sequence of the TM layers which is not totally respected in reality[28].

The Rietveld refinement also shows that Na^+ ions occupy both edge- and face-sharing prismatic sites in the ratio 2 :1 which is commonly observed in P2-type sodium layered oxides and a schematic representation of the structure is shown in Figure 1. Surprisingly, these results show a slight sodium deficit compared to the theoretical chemical formula $Na_{0.7}Li_{0.14}Ni_{0.14}Mn_{0.72}O_2$ and the experimental formula $Na_{0.66}Li_{0.15}Ni_{0.13}Mn_{0.71}O_2$ determined by ICP-OES chemical analysis. This has not been understood yet. The synchrotron X-ray diffraction pattern of this sodium layered oxide also exhibits features of Li_2MnO_3 impurity (1.2 weight %) at 2θ ≈ 7°. In addition, diffraction peaks of Na_2CO_3 impurity are also detected on the synchrotron X-ray diffraction pattern (1.0 weight %).

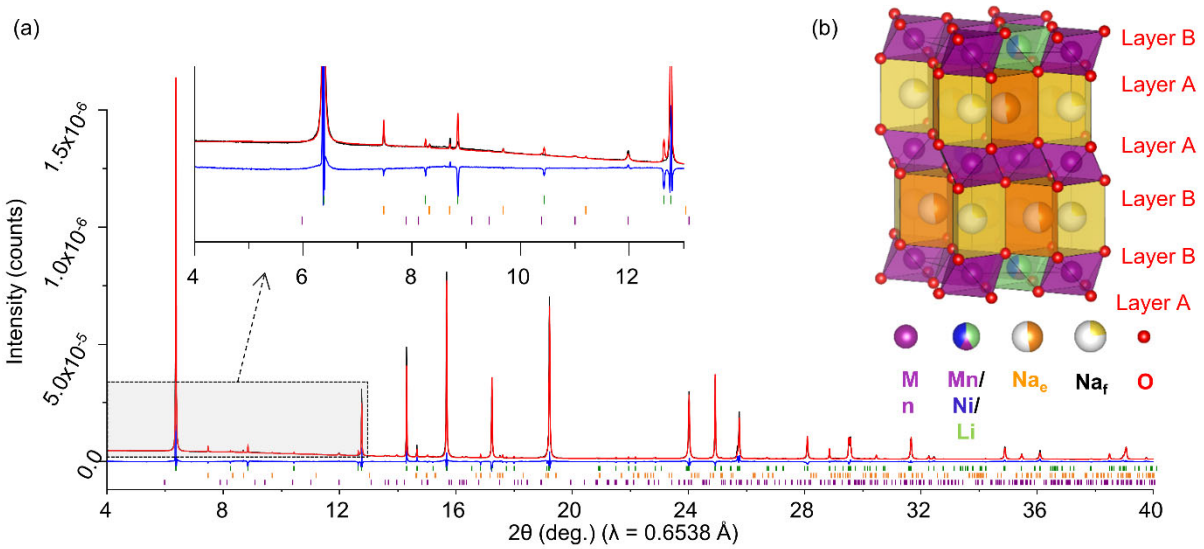

Figure 1. (a) Experimental (black line) and calculated using the Rietveld method (red line) synchrotron powder X-ray diffraction patterns of the P2-$Na_{0.7}[Li_{0.14}Ni_{0.14}Mn_{0.72}]O_2$ phase. The

blue line shows the difference between the experimental pattern and the calculated ones. Green, orange and purple vertical bars represent Bragg reflection positions for P2-$Na_{0.7}[Li_{0.14}Ni_{0.14}Mn_{0.72}]O_2$ (Space group: $P6_3$, a = 4.969 Å, c = 11.139 Å), Li_2MnO_3 (Space group: $C2/m$, a = 4.931 Å, b = 8.528 Å, c = 5.028 Å and β = 109.40°) and Na_2CO_3 (Space group: $C2/m$, a = 8.909 Å, b = 5.240 Å, c = 6.049 Å, β = 101.30°). (b) Three-dimensional representation of the structure of the P2-$Na_{0.7}[Li_{0.14}Ni_{0.14}Mn_{0.72}]O_2$ phase. The two sodium sites are both partially occupied.

The solid-state ion-exchange reaction from the sodium P2-type phase to the lithium O2-type phase was monitored by variable temperature X-ray diffraction from room temperature to 400°C. Only part of the diffraction patterns recorded during this experiment is shown in Figure 2(a). This part corresponds to the 2θ-range from 16°-24° which shows the characteristic reflection of the interlayer distance in layered oxides. The full diffraction patterns are shown in Supporting Information (Figure S1).

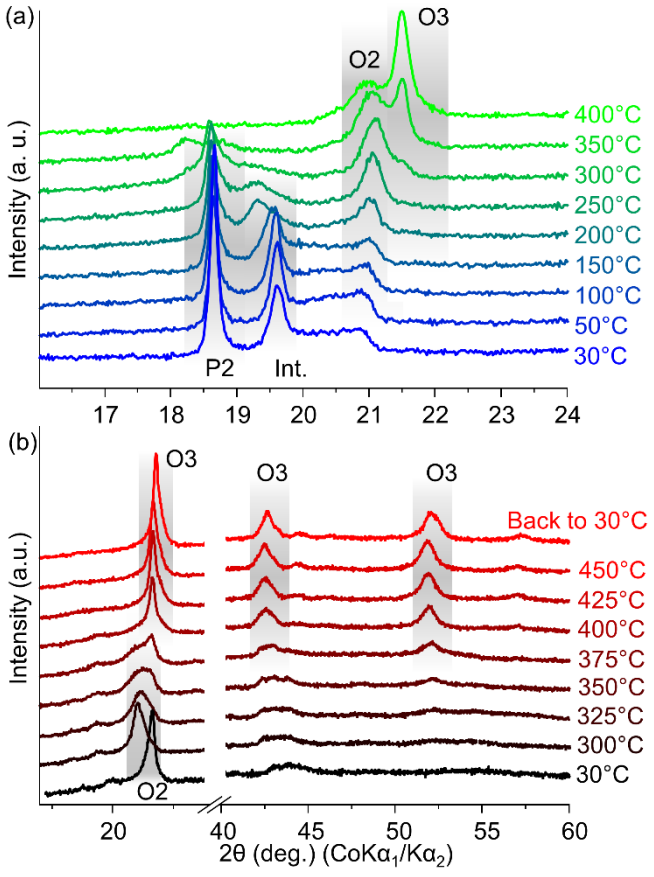

Figure 2. Variable temperature X-ray diffraction patterns recorded in a helium flow during (a) the ion-exchange reaction between 1 mole of P2-$Na_{0.7}[Li_{0.14}Ni_{0.14}Mn_{0.72}]O_2$ and 1.5 mole of LiCl and (b) the irreversible structural transition from the O2-$Li_{0.84}Ni_{0.14}Mn_{0.72}O_2$ to the O3-$Li_{0.84}Ni_{0.14}Mn_{0.72}O_2$ phase. The O2-$Li_{0.84}Ni_{0.14}Mn_{0.72}O_2$ phase was obtained prior to the variable temperature X-ray diffraction experiment and the residual salts LiCl and NaCl had been washed away using methanol. In (a) and (b), "P2", "O2" and "O3" labels are used to identify the different diffraction peaks belonging to the P2-$Na_{0.7}[Li_{0.14}Ni_{0.14}Mn_{0.72}]O_2$, O2-$Li_{0.84}Ni_{0.14}Mn_{0.72}O_2$ and O3-$Li_{0.84}Ni_{0.14}Mn_{0.72}O_2$ phases, respectively. The "Int." label is used to highlight the existence of an intermediate layered phase, containing sodium and lithium in its interlayer space.

In addition to the diffraction peak at $[2\theta_{Co}] \approx 18.6°$ (d = 5.52 Å) associated with the *002* reflection of sodium P2-type phase, it is worth noticing that the X-ray diffraction pattern recorded at 30 °C in dark blue already exhibits the presence of a second phase with a reflection at a higher angular position ($[2\theta_{Co}] \approx 19.6°$, d = 5.25 Å). The calculated interlayer distance in this second phase happens to be an intermediate distance between the interlayer distances commonly observed in sodium layered oxides (5.4 Å < d < 5.7 Å) and those of lithium layered oxides (4.7 Å < d < 5.0 Å). Its value is also close to the interreticular distance d_{004} of the OP4-$(Li_{0.42}Na_{0.37})CoO_2$ phase whose structure is built of TMO_6 layers, separated alternately by layers of sodium ions in prismatic sites and layers of lithium ions in octahedral sites[29,30]. Therefore, it is assumed that the Na^+-to-Li^+ ion-exchange reaction is already initiated during the grinding of the sodium P2-type phase with lithium chloride with the use of the mortar and pestle in the Ar-filled glovebox at room temperature. The existence of this intermediate layered phase, containing both sodium and lithium, has already been observed during the Na^+-to-Li^+ ion-exchange from $Na_{2/3}[Ni_{1/3}Mn_{2/3}]O_2$[21]. The intermediate phase is unlikely to be unique and

a wide range of intermediate compositions should be present in the mixture as shown by the broad shoulder in the 20-21° 2θ-range.

When the temperature increases, this broad shoulder gets narrower to become a single diffraction peak at 200 °C at $[2\theta_{Co}] \approx 21°$. This gives an interlayer distance of d = 4.90 Å for this new phase, which is consistent with that of an O2-type phase. Simultaneously, the intensity of the reflection related to the P2-type phase and the intermediate phase decreases, in good agreement with the growth of a new layered phase. From 300°C, a new diffraction peak appears at $[2\theta_{Co}] \approx 21.5°$ (which corresponds to an interlayer distance of 4.79 Å) and it can be attributed to the growth of an O3-type phase as a smaller interlayer distance is expected for an O3-type structure of the same composition. For example, the interlayer distance is d = 4.69 Å in O3-$LiCoO_2$, whereas it is 4.76 Å in O2-$LiCoO_2$[15]. Indeed, in the O2-type phases, the lithium ions occupy octahedral sites sharing both a face and edges with the TMO_6 octahedra, whereas they occupy sites sharing only edges with these same octahedra in the O3-type phases. Therefore, there are strong electrostatic repulsions between the lithium ions and the transition metal cations located in close proximity in O2-type phases and the interlayer space is larger to attenuate these repulsions.

At 400°C, the diffraction peak characteristic of the O3-type phase largely dominates, showing the metastability of the O2-type phase. This irreversible transformation from the O2-type phase to the O3-type phase was confirmed by a new variable temperature X-ray diffraction experiment. For this experiment, a pure O2-type phase was heated without the presence of LiCl salt. The X-ray diffraction patterns recorded during this experiment clearly show that the O2-type phase transforms into the O3-type phase from 325°C to completely disappear at 425°C (Figure 2(b)). These two experiments clearly show that the optimum temperature for obtaining the pure O2-type phase by solid-state ion-exchange is approximately 300°C.

Whereas the existence of the O2-type phase alone had not been observed during the variable temperature X-ray diffraction experiment, the heat treatment used for the ion-exchange at 300°C for 4 hours in the glass tube under vacuum was sufficient to obtain the pure O2-type phase. Chemical analysis performed by ICP-OES further confirmed that each sodium ion was indeed removed from the structure and replaced by the same amount of lithium ions; in addition, the Ni/Mn ratio remained identical, leading to the experimental formula of $Li_{0.84}Ni_{0.14}Mn_{0.72}O_2$. The chemical formula of the sodium phase is written $Na_{0.7}[Li_{0.14}Ni_{0.14}Mn_{0.72}]O_2$ to separate the prismatic sites occupied by sodium and the octahedral sites occupied by Li, Ni and Mn. In the lithium phase, all Li^+ ions occupy octahedral sites. Therefore, its chemical formula is written O2-$Li_{0.84}Ni_{0.14}Mn_{0.72}O_2$, where 0.84 mole of lithium per formula unit represents the sum of Li^+ ions in the $(Li,Ni,Mn)O_2$ layers and in the interslab space. X-ray absorption spectroscopy (XAS) at the Mn K-edge was also performed to determine the oxidation state of manganese ions in both the sodium and lithium layered oxides. XANES spectra at the Mn K-edge indicate that manganese ions are in their tetravalent state Mn(+IV) in the pristine sodium layered oxide as well as in the pristine lithium phase, suggesting that the oxidation state of this transition metal cation was not affected by the solid-state ion-exchange.

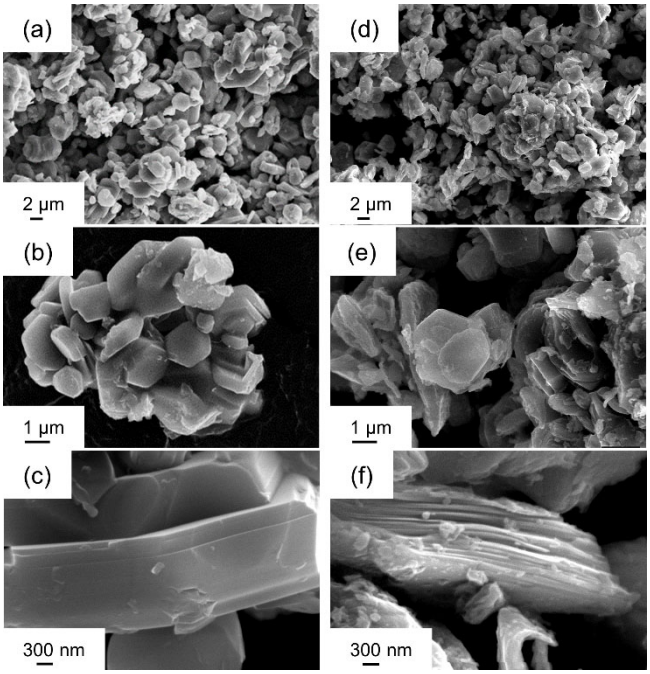

Figure 3: Scanning electron microscopy images of particles of: (a), (b) and (c) the P2-$Na_{0.7}[Li_{0.14}Ni_{0.14}Mn_{0.72}]O_2$ phase; (d), (e) and (f) the O2-$Li_{0.84}Ni_{0.14}Mn_{0.72}O_2$ phase.

As mentioned in the introduction, ion-exchange is a topotactic reaction which involves only a slight reorganization of the crystal structure. The shape and the size of the particles after the exchange are therefore mostly preserved as shown in Figure 3. The crystallites in the P2-type sodium layered oxide exhibit hexagonal platelets (Figure 3(a)), in good agreement with their crystal structure. Their dimensions vary from 0.5 to 5 µm in width and from 0.1 to 1 µm in thickness (Figure 3(b)). Their surface and their edges are smooth, characteristic of a crystalline material without apparent defects or impurities (Figure 3(c)). An elemental analysis by Energy Dispersive X-ray Spectroscopy (EDS) mapping highlighted a homogeneous chemical composition in all the particles. By comparison, the crystallites in the O2-type lithium layered oxide show a similar morphology: the hexagonal pellet-shaped particles remain, and the grains are still of micrometric dimensions (Figures 3(d) and 3(e)).

However, one can notice that the surface of the particles is different: the hexagonal particles in the O2-type lithium layered oxide show some smaller particles at their surface (Figure 3(f)).

An EDS mapping on several areas of the sample shows that these are not residual NaCl salts. It is assumed that the ion-exchange reaction may have generated mechanical strains strong enough to cause the crystallites to crack and small fragments to break off. This hypothesis is further supported by the exfoliated aspect of the platelet edges: originally very smooth on the P2-type sodium phase (Figure 3(c)), they appear strongly uneven and damaged on the lithium phase with a step-like structure (Figure 3(f)). The O2-type lithium phase probably nucleates at different points of the same particle. Its growth imposes glides of the (Li,Ni,Mn)O_2 layers which start at different nucleation points. At the junction of two growth fronts, these displacements can generate mechanical strains throughout the material, which are then responsible for microscopically visible changes.

The structural rearrangements occurring at the atomic scale during the ion-exchange were studied by synchrotron powder X-ray diffraction. The pattern of the O2-type lithium phase is shown in Figure 4(a). The main diffraction peaks can be indexed with the cell parameters a = 2.865(9) Å and c = 9.637(6) Å in the $P6_3mc$ space group (n°186) of conventional O2-type structures[18,19,22,28]. The synchrotron X-ray diffraction pattern of O2-type phase still exhibits the Li_2MnO_3 impurity which remained inert during the ion-exchange and the washing process. The diffraction peaks of Na_2CO_3 impurity are no longer visible on the diffraction pattern. However, a new Li_2CO_3 impurity was formed. Li_2CO_3 being less soluble in methanol than Na_2CO_3, it is supposed to have precipitated during the washing step from CO_3^{2-} anions resulting from the dissolution of Na_2CO_3 and Li^+ ions resulting from the LiCl introduced in excess.

A strong anisotropic broadening of the diffraction peaks of the O2-type phase is clearly observed on the synchrotron X-ray diffraction pattern. This is commonly observed for O2-type layered oxides obtained by ion-exchange and it is associated with the presence of stacking faults along the c-axis. Previous works have already reported the theoretical ion-exchange mechanism from a P2-type sodium phase to an O2-type lithium phase[15,16,28]. Since the ionic

radius of Li^+ is smaller than that of Na^+, lithium ions are not stabilized and cannot occupy trigonal prismatic sites. For that reason, the ion-exchange results in the planar and local translation of $(Li,Ni,Mn)O_2$ layers towards various directions to create octahedral sites for lithium ions where they are more stabilized. The gliding of $(Li,Ni,Mn)O_2$ layers can occur along 6 different directions (Figure S2 in Supporting information). Among these 6 glides, 3 lead to the same oxygen packing (ABAC), the 3 others to another one (ABCB). It can be assumed that none of these glides is much more favorable than the others. Therefore, they are not necessarily cooperative and they can occur along all 6 directions with similar probability. They do not lead to an ideal O2-type structure. Indeed, the formation of the latter would require that one $(Li,Ni,Mn)O_2$ layer out of two glides exactly along the same direction, or at least, along a direction leading to the same oxygen packing.

In order to better estimate the nature and the amount of stacking faults present in the O2-type lithium-rich layered oxide obtained by ion-exchange, several series of SRXD patterns were simulated with the *Faults* program attached to the *Fullprof* suite[31]. Approximately one hundred diagrams were simulated considering probabilities of faults ranging from 0% to 100%. All the details of the simulations are given in Supporting Information. The simulated synchrotron X-ray diffraction pattern that best matches the experimental one in terms of relative intensities and peaks broadening is shown in Figure 4(a). It was obtained by considering a probability of stacking fault of 40%. The structure of the $Li_{0.84}Ni_{0.14}Mn_{0.72}O_2$ compound studied here is therefore far from an ideal O2-type structure. The weak diffraction peak visible at $2\theta \approx 10°$ on this experimental synchrotron X-ray diffraction pattern is well simulated, indicating that the in-plane ordering of cations in the $(Li,Ni,Mn)O_2$ layers is maintained after the ion-exchange reaction. In addition, its tailed-shape suggests that the cations in these layers are randomly distributed along the c-axis.

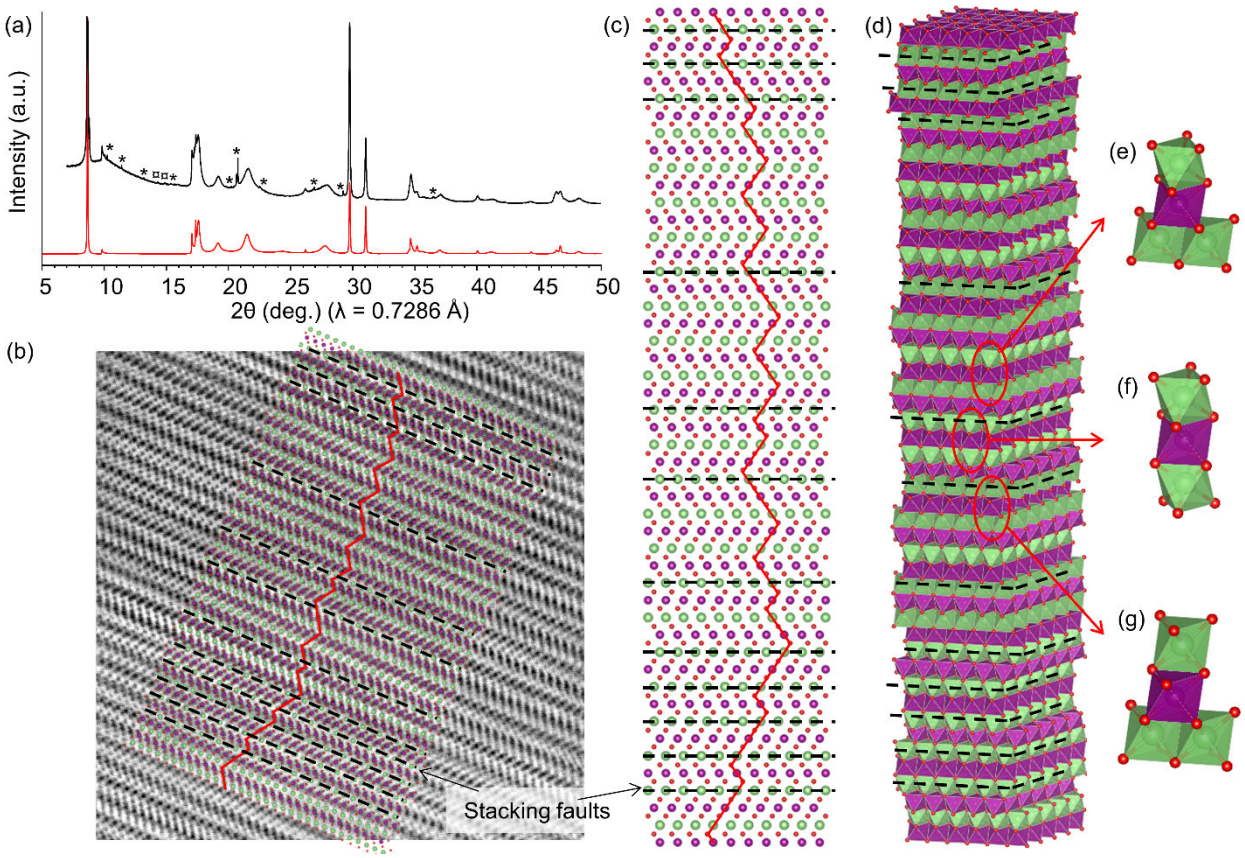

Figure 4. (a) Experimental (black line) and simulated using *Faults* program (red line) synchrotron X-ray diffraction patterns for O2-$Li_{0.84}Ni_{0.14}Mn_{0.72}O_2$ phase. Li_2MnO_3 and Li_2CO_3 impurity diffraction peaks are highlighted with * and ¤ symbols, respectively. (b) ABF-STEM image. (c) Projection and (d) three-dimensional representation of the structure determined from the ABF-STEM image: Li,Ni and Mn atoms located in the (Li,Ni,Mn)O_2 layers are shown in purple, lithium in the interlayer space is shown in green. (e), (f) and (g) Possible local environments for (Li,Ni,Mn)O_6 octahedra. For (b), (c) and (d), please note that the interlayer space is supposedly only partially occupied by lithium ions, but for simplicity all sites possibly occupied by lithium are shown in green. Stacking fault occurrence is represented with a black dashed line.

The existence of stacking faults in the compound was confirmed by High-resolution Transmission Electron Microscopy. The ABF-STEM image shown in Figure 4(b) indicates that

the $Li_{0.84}Ni_{0.14}Mn_{0.72}O_2$ compound contains some domains where the O2-type stacking is perfect, but these domains are made of only a few $(Li,Ni,Mn)O_2$ layers. It appears that the direction of the glidings of these layers is not cooperative and they occur randomly according to one of the 6 directions defined above. Statistical analyses of the three ABF-STEM images recorded on different particles of the $Li_{0.84}Ni_{0.14}Mn_{0.72}O_2$ compound show that the probability of stacking faults occurring with respect to an ideal O2-type structure is about 40%, in good agreement with the results previously obtained in the *Faults* simulation.

The random gliding of the $(Li,Ni,Mn)O_2$ layers has the consequence of creating various environments for the TM ions. Indeed, TMO_6 octahedra can either share edges on one side and a face on the other side with LiO_6 octahedra (as it is the case in the ideal O2-type structure), or share only edges with LiO_6 octahedra (like in O3-type structure), or share only one face on each side with two LiO_6 octahedra. The lithium ion environment, on the other hand, is always the same: the LiO_6 octahedra share edges with an TMO_6 octahedron on one side and a face with another TMO_6 octahedron on the other side.

The O2-$Li_{0.84}Ni_{0.14}Mn_{0.72}O_2$ phase was then used as the positive electrode material in a lithium battery to study its electrochemical properties. The charge/discharge galvanostatic curves recorded at C/20 between 2.6V and 4.6V are shown in Figure 5. At first, upon the first charge, nickel ions were thought to be oxidized from Ni^{2+} to Ni^{4+}, contributing to the deintercalation of 0.28 mole of Li^+ per formula unit $Li_xNi_{0.14}Mn_{0.72}O_2$. Then, the electrochemical curve exhibits a potential "plateau" starting at approximately 4.4V vs. Li^+/Li and associated with the oxidation of oxygen O^{2-} to $O^{\delta-}$ (where $\delta < 2$) (the exact nature of the oxidized species of oxygen not having been studied within the framework of this work, that is why this one is noted $O^{\delta-}$), which is a typical feature of the first charge in Li-rich layered oxides. The derivative curve dQ/dV (Figure 5.c) shows two distinct peaks at 3.9V and 4.4V respectively, indicating that those two redox reactions are successive upon first charge.

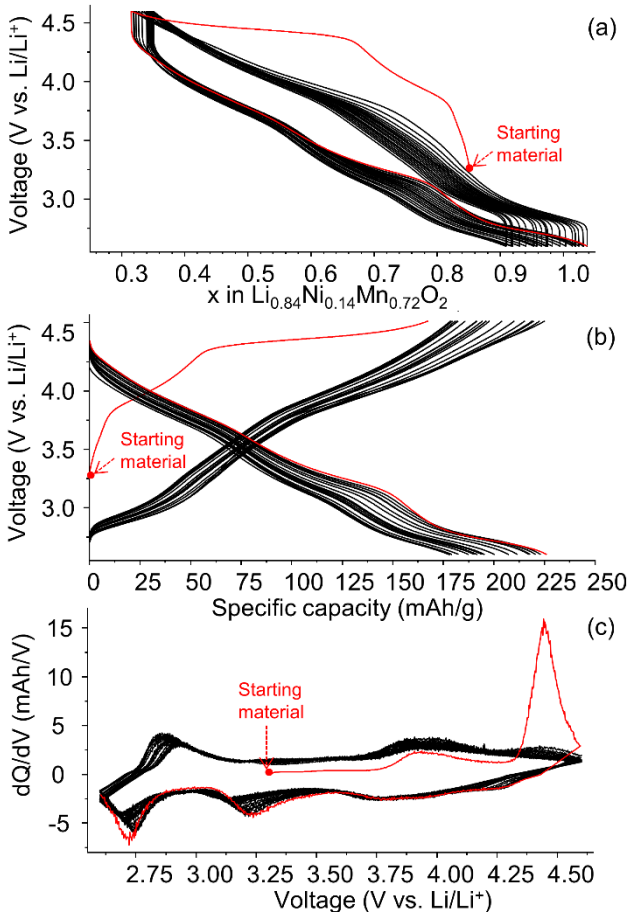

Figure 5. 20 galvanostatic cycles of charge and discharge of a lithium battery cell using the O2-$Li_{0.84}Ni_{0.14}Mn_{0.72}O_2$ phase at the positive electrode. The first cycle is shown in red. (a) Evolution of the cell voltage V as a function of the lithium content x in O2-$Li_xNi_{0.14}Mn_{0.72}O_2$. (b) Evolution of the cell voltage V as a function of the capacity of the battery. (c) Evolution of the derivative curve dQ/dV as a function of the cell voltage V.

During the consecutive discharge, lithium ions are intercalated up to 1.04 moles of Li^+ per formula unit, beyond the initial lithium content of 0.84 mole Li^+, which was expected considering that the starting material O2-$Li_{0.84}Ni_{0.14}Mn_{0.72}O_2$ contained vacancies in the interlayer space. Consequently, the positive electrode material delivers a large specific capacity of 225 mAh/g. The reduction of nickel ions to Ni^{2+} state and the partial reduction of manganese ions to Mn^{3+} is visible on the dQ/dV curves with two peaks at 3.8V and 2.7V, respectively. An additional peak is also observed at 3.2V (Figure 5(c)). In light of recent XAS results reported

by Kawai *et al*.[32] on a similar O2-type Li-rich layered oxide, this third anodic dQ/dV peak is attributed to the reversible reduction of oxygen ions upon discharge. While the oxygen-redox reactions occur simultaneously with the cationic-redox reactions for most O3-type Li-rich layered oxides, the redox reactions in this O2-type Li-rich layered oxide appear to be successive.

The following charge/discharge curves significantly deviate from the first cycle. In particular, the large voltage plateau upon charge is no longer visible, indicating that the redox mechanisms involved in the first cycle are different than those occurring in the following cycles. However, the dQ/dV curve seems to show that the $O^{2-}/O^{\delta-}$ couple is still active during this second charge, with the residual presence of a low intensity peak at 4.5 V in oxidation/ 4.4 V in reduction. It would therefore be likely that the anionic redox of oxygen is at least partially reversible. The progressive loss of intensity of these oxidation and reduction peaks upon cycling highlights the loss of capacity coming from the oxygen redox. This could be due, for example, to structural rearrangements, or even to the loss of oxygen at the surface of the material. Eventually, the specific capacity decreases down to 175 mAh/g at the 20^{th} cycle (i.e. a decrease of approximately 30% compare to the first discharge). A C-rate test was conducted for C-rates from C/50 to C/2 and it showed that this specific capacity considerably decreases when the current reaches C-rates of C/2 or more (Figure S5 in Supporting Information).

In order to better understand the structural mechanisms induced during battery cycling, *operando* X-ray diffraction experiments were performed during the first charge and discharge cycles. The X-ray diffraction patterns recorded in our laboratory during the first charge and discharge are given in Figure 6. The lab-made electrochemical cell which was used for the experiment has a much higher resistance that the coin cells used for galvanostatic cells. Therefore, the polarization was very high and voltage floating wasapplied at the end of the charge and discharge to force the lithium electrochemical deintercalation and intercalation,

respectively. Due to preferred orientation of the particles in the self-supported electrode used for this experiment and the broadness of the other diffraction peaks, only the *"002"* reflection, corresponding to the interlayer distance, was visible on the X-ray diffraction pattern and recorded. Moreover, to limit the duration of the use of the diffractometer for this experiment, the battery was discharged first, off the diffractometer, and it was placed in the diffractometer once the discharged state was reached. During the first charge, the interlayer distance decreases continuously as the "*002"* reflection continuously shifts towards higher 2θ values. Such an evolution goes against the behavior generally observed for O3-type layered oxides for which an increase in the interlayer distance is usually observed when the lithium deintercalation starts. When the lithium content becomes low ($x_{Li+} < 0.25$ in Li_xMO_2), the O3-type layered oxides undergo a phase transition towards a O1-type structure by the gliding of the MO_2 layers, causing a sudden and sharp drop in the interlayer distance[33,34]. In the case of the O2-$Li_{0.84}Ni_{0.14}Mn_{0.72}O_2$ phase, another feature dominates. As the lithium is deintercalated from the interlayer space, there are fewer transition metal cations located in the $(Li,Ni,Mn)O_2$ layers facing a Li^+ ion of the interlayer space. Therefore, there are less electrostatic repulsions and the interlayer distance decreases. Moreover, no sharp decrease in the interlayer distance is observed at the end of charge as the transition from a O2- to O1-type structure is not possible at room temperature. The smooth variation in the interlayer distance also indicates that the O2-$Li_{0.84}Ni_{0.14}Mn_{0.72}O_2$ phase does not transform into a $T^{\#}2$-type structure phase upon lithium deintercalation, which would have significantly larger interlayer distance, unlike O2-$LiCoO_2$[35].

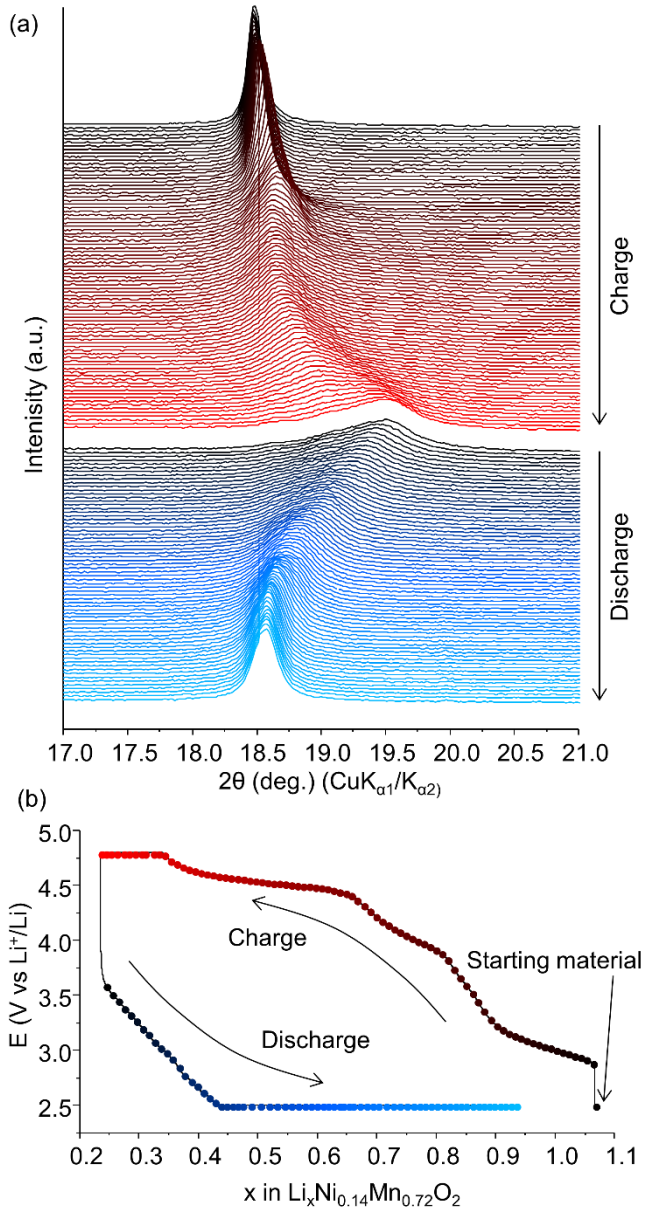

Figure 6. *Operando* X-ray diffraction experiment. (a) X-ray diffraction patterns collected during the first charge and the first full discharge of a lithium battery cell using the O2-$Li_{0.84}Ni_{0.14}Mn_{0.72}O_2$ phase at the positive electrode. (b) Galvanostatic electrochemical curve recorded at a rate of C/50 during the *operando* experiment. The colored dots highlight the state of charge of the different $Li_xNi_{0.14}Mn_{0.72}O_2$ phases whose X-ray diffraction patterns are shown in (a). To force the lithium electrochemical deintercalation and intercalation, voltage floating was applied at 4.6 V and 2.5 V at the end of the charge and discharge, respectively.

At the end of the charge, the *"002"* diffraction line is very broad and it seems to present two peaks. This indicates the presence of two phases at the end of the lithium deintercalation; however, these two phases could not be clearly identified. The X-ray diffraction patterns collected during battery discharge follow the opposite trend: the *"002"* diffraction line moves reversibly towards smaller 2θ values, indicating an increase in the interlayer distance. This *operando* X-ray diffraction experiment shows that the O2-type structure is stable after a first cycle of lithium electrochemical de- and intercalation. Finally, *ex situ* full X-ray diffraction patterns recorded after 3 cycles of charge and discharge confirm that the O2-type structure was stable upon cycling.

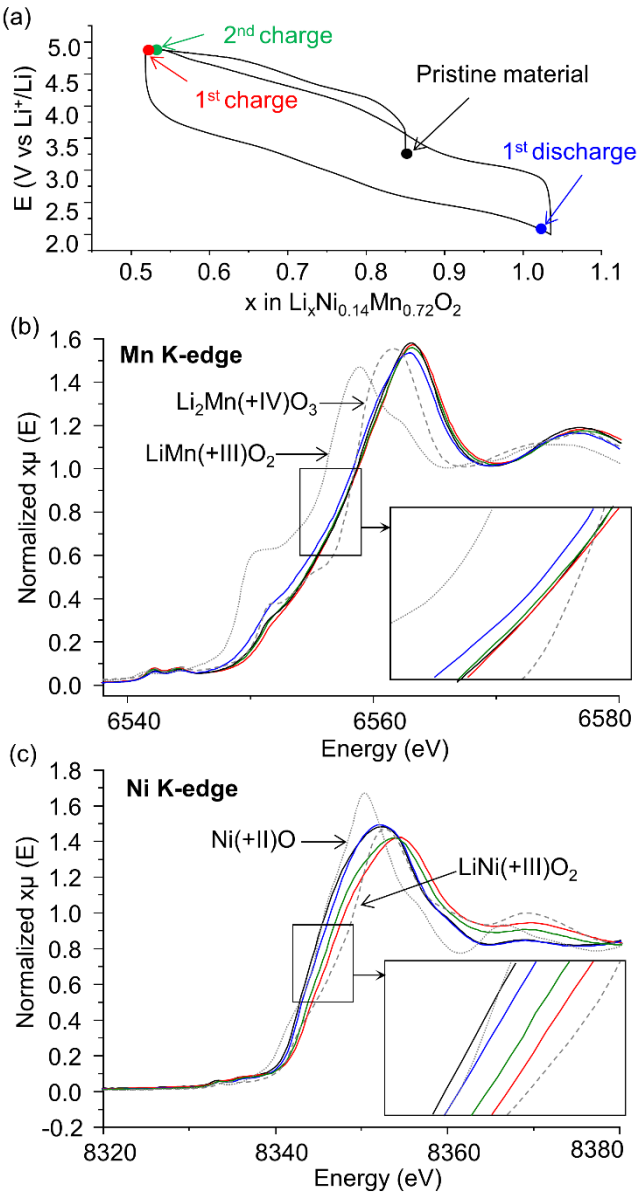

Figure 7. *Operando* X-ray absorption spectroscopy experiment. (a) Galvanostatic electrochemical curve recorded at a rate of C/20 during the *operando* XAS experiment of a lithium battery cell using the O2-$Li_{0.84}Ni_{0.14}Mn_{0.72}O_2$ phase at the positive electrode. The colored dots highlight the state of charge of the different $Li_xNi_{0.14}Mn_{0.72}O_2$ phases whose X-ray absorption spectra are shown in (b) and (c). (b) and (c) Spectra recorded at the Mn and Ni K-edges, respectively, for the four different phases highlighted in (a). Spectra for different reference compounds containing Mn^{3+} or Mn^{4+} ions and Ni^{2+} and Ni^{3+} ions are also shown.

The redox mechanisms occurring during this first cycle of lithium electrochemical de- and intercalation were studied by *operando* X-ray absorption spectroscopy (XAS) at nickel and manganese K-edge. In the initial state, before the first charge, the XAS spectra recorded on the O2-$Li_xNi_{0.14}Mn_{0.72}O_2$ phase at Ni and Mn K-edge confirm that these two transition elements are at oxidation state +II and +IV, respectively (Figure 7(b) and (c)). During the first charge, the absorption spectra at Mn K-edge barely evolve as shown in Figure 8(b) (the evolution of Ni- and K-edges for two specific absorption intensities are shown in Supporting Information). This confirms that the manganese remains electrochemically inactive throughout the first charge. On the other hand, the nickel absorption edge gradually shifts towards higher energies during the lithium electrochemical deintercalation, showing the continuous oxidation of nickel. When the lithium content reaches $x \approx 0.6$ in the O2-$Li_xNi_{0.14}Mn_{0.72}O_2$ phase, the evolution of this edge is much less marked. This composition is close to the limit composition expected if the electrochemical deintercalation of lithium was only compensated by the successive oxidation of nickel ions to Ni^{3+}, then Ni^{4+}. However, the last spectrum recorded at the end of the charge is close to the spectrum recorded for LiNi(III)O_2 (Figure 7(c)). It therefore seems that the oxidation of nickel stops at oxidation state +III. This is in agreement with the electrochemical curve shown in Figure 5(a): the plateau associated with the oxygen oxidation indeed appears for a lithium content $x \approx 0.67$ in O2-$Li_xNi_{0.14}Mn_{0.72}O_2$, far from the content expected after complete oxidation of Ni^{2+} to Ni^{4+}, $x \approx 0.56$.

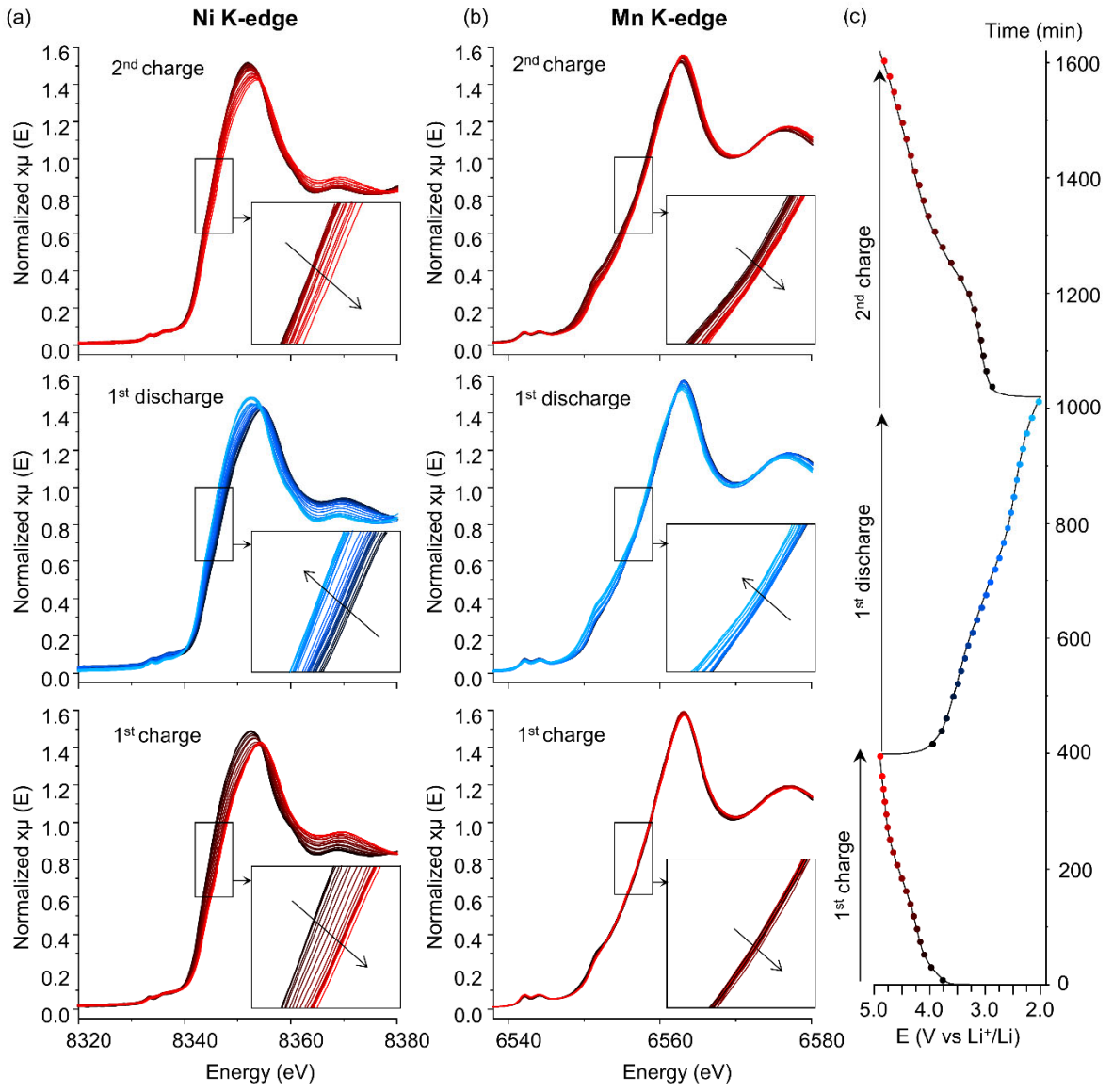

Figure 8. *Operando* X-ray absorption spectra recorded at the (a) Ni and (b) Mn K-edges during the first lithium electrochemical de- and intercalation cycle of the O2-$Li_{0.84}Ni_{0.14}Mn_{0.72}O_2$ phase. (c) Galvanostatic electrochemical curve recorded at a rate of C/20 during the *operando* experiment. The colored dots correspond to the different acquisitions of the spectra.

The limited oxidation of nickel up to oxidation state +III only seems to be specific to this O2-type lithium rich layered oxide as several *ex situ* and *operando* XAS experiments on different compounds having similar compositions but with an O3-type structure showed that nickel is oxidized to Ni^{4+} at the end of charge[36,37]. This tends to confirm the participation of

the oxygen oxidation in order to extract the lithium ions from the layered structure to reach the composition $Li_{\approx 0.52}Ni_{0.14}Mn_{0.72}O_2$ at the end of the first charge. During the first electrochemical deintercalation of lithium from the compound with an O2-type structure, there would therefore be the successive oxidation of nickel and then of oxygen, thus confirming the results provided by electrochemistry (Figure 5(c)). The electrical resistance of the electrochemical cell used for the *operando* XAS experiments was unfortunately larger than that of coin cells used in the laboratory, further lithium extraction was not possible.

During the first discharge, the Ni absorption edge shifts progressively and reversibly towards lower energies (Figure 8(a)), indicating that the nickel ions are reduced to the composition $Li_{\approx 0.91}Ni_{0.14}Mn_{0.72}O_2$, composition from which the position of the Ni absorption edge stops shifting. Their oxidation state determined at the end of the discharge is +II, as expected (Figure 7(c)). While it had remained unchanged throughout the first part of the first discharge, the Mn absorption edge begins to shift towards lower energies from the composition $Li_{\approx 0.87}Ni_{0.14}Mn_{0.72}O_2$. The evolution of the two absorption edges, Ni and Mn K-edges, clearly show that the couples Ni^{3+}/Ni^{2+} and Mn^{4+}/Mn^{3+} are successively electrochemically active during the discharge. However, the absorption spectrum recorded at the Mn K-edge at the end of the discharge (Figure 7(b)) is very close to that recorded for the pristine material. This shows that the manganese was only very partially reduced. The reduction alone of 0.14 mole of Ni^{3+} to Ni^{2+} and of very small amount of Mn^{4+} to Mn^{3+} does not explain the intercalation of more than 0.5 mole of lithium per formula unit during the discharge. The reintercalation of lithium is therefore made possible thanks to the reversible reduction of oxygen. During the second charge, the evolution of the Ni and Mn K-edge absorption spectra shows that the oxidation of the transition metal ions is successive (Figure 8), the oxidation of manganese at the start of the charge is followed by that of nickel. At the end of the second discharge, it appears that the Ni absorption edge is located at lower energies (Figure 7(c)) than that recorded for approximately

the same composition at the end of the first charge (Figure 7(a)). This difference could indicate that the oxidation of oxygen started before the end of the oxidation of nickel, contrary to what was observed during the first charge. The oxidations of nickel and oxygen during the second charge and beyond would therefore be at least partially concomitant. This could explain the large peak observed in oxidation on the derivated curve dQ/dV around 4.0 V which could be the overlap of the oxidation peak of Ni^{2+} ions into Ni^{3+} and of some oxygen ions O^{2-} into $O^{\delta-}$. Finally, even if the *operando* X-ray absorption spectroscopy experiments were only carried out on the first charge and the second charge, the redox processes occurring during the following cycles must be very similar, the shape of the electrochemical curve no longer changing after the first charge. It showed that a large part of the capacity obtained upon cycling relies on the oxygen redox which is also reversible upon cycling.

Conclusion

In this article, a new synthesis route of lithium-rich layered oxide with an O2-type structure has been reported: it is a solid-state ion-exchange consisting of mixing a P2-type sodium phase with LiCl. The structure of the O2-type phase thus obtained contains numerous stacking faults linked to the structural mechanisms involved during the ion exchange: the layers formed by MO_6 octahedra (with M = Li, Ni and Mn) slide in a non-cooperative way to generate octahedral sites that lithium ions can occupy. The use of the O2-$Li_{0.84}Ni_{0.14}Mn_{0.72}O_2$ phase used as positive electrode material in a lithium battery has shown that the latter can deliver a high specific capacity (more than 220 mAh/g), based on the reversible redox reactions of the couples Ni^{2+}/Ni^{3+}, Mn^{3+}/Mn^{4+} and $O^{2-}/O^{\delta-}$. The exact nature of the oxidized species has not been determined but will be the subject of further study in the future. The good capacity retention is therefore not only based on a good reversibility of the redox reactions (anionic and cationic redox) but also on a good structural stability at room temperature of the O2-type structure

which does not undergo any significant structural transitions upon cylcling involving abrupt unit cell parameter changes.

ASSOCIATED CONTENT

Supporting Information. The various figures mentioned under the name "Figure Sx" in the manuscript are all available in a single document. The parameters used for the simulation of the X-ray diffraction pattern with the program *Faults* are also given in this file.

AUTHOR INFORMATION

* marie.guignard@icmcb.cnrs.fr

Author Contributions

The manuscript was written through contributions of all authors. All authors have given approval to the final version of the manuscript.

ACKNOWLEDGMENT

VS and MG would like to thank the *Faults* Team for providing them with a version of the *Faults* program to work with up to 50 sheets.

REFERENCES

(1) Sovacool, B. K. The Precarious Political Economy of Cobalt: Balancing Prosperity, Poverty, and Brutality in Artisanal and Industrial Mining in the Democratic Republic of the Congo. *The Extractive Industries and Society* **2019**, *6* (3), 915–939. https://doi.org/10.1016/j.exis.2019.05.018.

(2) Lu, Z.; Dahn, J. R. Structure and Electrochemistry of Layered $Li[Cr_xLi_{(1/3-x/3)}Mn_{(2/3-2x/3)}O_2$. *J. Electrochem. Soc.* **2002**, *149* (11), A1454. https://doi.org/10.1149/1.1513557.

(3) Lu, Z.; Dahn, J. R. Understanding the Anomalous Capacity of $Li/Li[Ni_xLi_{(1/3-2x/3)}Mn_{(2/3-x/3)}O_2$ Cells Using In Situ X-Ray Diffraction and Electrochemical Studies. *J. Electrochem. Soc.* **2002**, *149* (7), A815. https://doi.org/10.1149/1.1480014.

(4) Johnson, C. S.; Li, N.; Lefief, C.; Thackeray, M. M. Anomalous Capacity and Cycling Stability of $xLi_2MnO_3 \cdot (1-x)LiMO_2$ Electrodes (M=Mn, Ni, Co) in Lithium Batteries at 50°C. *Electrochem. Commun.* **2007**, *9* (4), 787–795. https://doi.org/10.1016/j.elecom.2006.11.006.

(5) Yabuuchi, N.; Yoshii, K.; Myung, S.-T.; Nakai, I.; Komaba, S. Detailed Studies of a High-Capacity Electrode Material for Rechargeable Batteries, $Li_2MnO_3-LiCo_{1/3}Ni_{1/3}Mn_{1/3}O_2$. *J. Am. Chem. Soc.* **2011**, *133* (12), 4404–4419. https://doi.org/10.1021/ja108588y.

(6) Koga, H.; Croguennec, L.; Mannessiez, P.; Ménétrier, M.; Weill, F.; Bourgeois, L.; Duttine, M.; Suard, E.; Delmas, C. $Li_{1.20}Mn_{0.54}Co_{0.13}Ni_{0.13}O_2$ with Different Particle Sizes as Attractive Positive Electrode Materials for Lithium-Ion Batteries: Insights into Their Structure. *J. Phys. Chem. C* **2012**, *116* (25), 13497–13506. https://doi.org/10.1021/jp301879x.

(7) Koga, H.; Croguennec, L.; Ménétrier, M.; Douhil, K.; Belin, S.; Bourgeois, L.; Suard, E.; Weill, F.; Delmas, C. Reversible Oxygen Participation to the Redox Processes Revealed for $Li_{1.20}Mn_{0.54}Co_{0.13}Ni_{0.13}O_2$. *J. Electrochem. Soc.* **2013**, *160* (6), A786–A792. https://doi.org/10.1149/2.038306jes.

(8) Koga, H.; Croguennec, L.; Ménétrier, M.; Mannessiez, P.; Weill, F.; Delmas, C. Different Oxygen Redox Participation for Bulk and Surface: A Possible Global Explanation for the

Cycling Mechanism of $Li_{1.20}Mn_{0.54}Co_{0.13}Ni_{0.13}O_2$. *J. Power Sources* **2013**, *236*, 250–258. https://doi.org/10.1016/j.jpowsour.2013.02.075.

(9) Koga, H.; Croguennec, L.; Ménétrier, M.; Mannessiez, P.; Weill, F.; Delmas, C.; Belin, S. Operando X-Ray Absorption Study of the Redox Processes Involved upon Cycling of the Li-Rich Layered Oxide $Li_{1.20}Mn_{0.54}Co_{0.13}Ni_{0.13}O_2$ in Li Ion Batteries. *J. Phys. Chem. C* **2014**, *118* (11), 5700–5709. https://doi.org/10.1021/jp412197z.

(10) Sathiya, M.; Abakumov, A. M.; Foix, D.; Rousse, G.; Ramesha, K.; Saubanère, M.; Doublet, M. L.; Vezin, H.; Laisa, C. P.; Prakash, A. S.; Gonbeau, D.; VanTendeloo, G.; Tarascon, J.-M. Origin of Voltage Decay in High-Capacity Layered Oxide Electrodes. *Nat. Mater.* **2015**, *14* (2), 230–238. https://doi.org/10.1038/nmat4137.

(11) Hong, J.; Gent, W. E.; Xiao, P.; Lim, K.; Seo, D.-H.; Wu, J.; Csernica, P. M.; Takacs, C. J.; Nordlund, D.; Sun, C.-J.; Stone, K. H.; Passarello, D.; Yang, W.; Prendergast, D.; Ceder, G.; Toney, M. F.; Chueh, W. C. Metal–Oxygen Decoordination Stabilizes Anion Redox in Li-Rich Oxides. *Nat. Mater.* **2019**, *18* (3), 256–265. https://doi.org/10.1038/s41563-018-0276-1.

(12) Gent, W. E.; Lim, K.; Liang, Y.; Li, Q.; Barnes, T.; Ahn, S.-J.; Stone, K. H.; McIntire, M.; Hong, J.; Song, J. H.; Li, Y.; Mehta, A.; Ermon, S.; Tyliszczak, T.; Kilcoyne, D.; Vine, D.; Park, J.-H.; Doo, S.-K.; Toney, M. F.; Yang, W.; Prendergast, D.; Chueh, W. C. Coupling between Oxygen Redox and Cation Migration Explains Unusual Electrochemistry in Lithium-Rich Layered Oxides. *Nat. Commun.* **2017**, *8* (1), 2091. https://doi.org/10.1038/s41467-017-02041-x.

(13) Eum, D.; Kim, B.; Kim, S. J.; Park, H.; Wu, J.; Cho, S.-P.; Yoon, G.; Lee, M. H.; Jung, S.-K.; Yang, W.; Seong, W. M.; Ku, K.; Tamwattana, O.; Park, S. K.; Hwang, I.; Kang, K. Voltage Decay and Redox Asymmetry Mitigation by Reversible Cation Migration in Lithium-

Rich Layered Oxide Electrodes. *Nat. Mater.* **2020**, *19* (4), 419–427. https://doi.org/10.1038/s41563-019-0572-4.

(14) Delmas, C.; Fouassier, C.; Hagenmuller, P. Structural Classification and Properties of the Layered Oxides. *Physica B+C* **1980**, *99* (1–4), 81–85. https://doi.org/10.1016/0378-4363(80)90214-4.

(15) Delmas, C.; Braconnier, J.-J.; Hagenmuller, P. A New Variety of $LiCoO_2$ with an Unusual Oxygen Packing Obtained by Exchange Reaction. *Mater. Res. Bull.* **1982**, *17* (1), 117–123. https://doi.org/10.1016/0025-5408(82)90192-1.

(16) Paulsen, J. M.; Thomas, C. L.; Dahn, J. R. Layered Li-Mn-Oxide with the O2 Structure: A Cathode Material for Li-Ion Cells Which Does Not Convert to Spinel. *J. Electrochem. Soc.* **1999**, *146* (10), 3560. https://doi.org/10.1149/1.1392514.

(17) Umeno, H.; Kawai, K.; Nishimura, S.; Asakura, D.; Okubo, M.; Yamada, A. Lithium-Rich O2-Type $Li_{0.66}[Li_{0.22}Ru_{0.78}]O_2$ Positive Electrode Material. *J. Electrochem. Soc.* **2022**, *169* (4), 040536. https://doi.org/10.1149/1945-7111/ac6459.

(18) Paulsen, J. M.; Mueller-Neuhaus, J. R.; Dahn, J. R. Layered $LiCoO_2$ with a Different Oxygen Stacking (O2 Structure) as a Cathode Material for Rechargeable Lithium Batteries. *J. Electrochem. Soc.* **2000**, *147* (2), 508. https://doi.org/10.1149/1.1393225.

(19) Carlier, D.; Saadoune, I.; Croguennec, L.; Ménétrier, M.; Suard, E.; Delmas, C. On the Metastable O2-Type $LiCoO_2$. *Solid State Ionics* **2001**, *144* (3–4), 263–276. https://doi.org/10.1016/S0167-2738(01)00982-1.

(20) Shang, H.; Zuo, Y.; Shen, F.; Song, J.; Ning, F.; Zhang, K.; He, L.; Xia, D. O2-Type $Li_{0.78}[Li_{0.24}Mn_{0.76}]O_2$ Nanowires for High-Performance Lithium-Ion Battery Cathode. *Nano Lett.* **2020**, *20* (8), 5779–5785. https://doi.org/10.1021/acs.nanolett.0c01640.

(21) Paulsen, J. M.; Larcher, D.; Dahn, J. R. O2 Structure $Li_{2/3}[Ni_{1/3}Mn_{2/3}]O_2$: A New Layered Cathode Material for Rechargeable Lithium Batteries III. Ion Exchange. *J. Electrochem. Soc.* **2000**, *147* (8), 2862. https://doi.org/10.1149/1.1393617.

(22) Mortemard de Boisse, B.; Jang, J.; Okubo, M.; Yamada, A. Cobalt-Free O2-Type Lithium-Rich Layered Oxides. *J. Electrochem. Soc.* **2018**, *165* (16), A3630–A3633. https://doi.org/10.1149/2.1331814jes.

(23) Tarascon, J. M. $Li_xMo_2O_4$: A New Promising Cathode Material for Secondary Lithium Cells. *J. Electrochem. Soc.* **1987**, *134* (6), 1345–1351. https://doi.org/10.1149/1.2100671.

(24) Paulsen, J. M.; Dahn, J. R. O2-Type $Li_{2/3}Ni_{1/3}Mn_{2/3}O_2$: A New Layered Cathode Material for Rechargeable Lithium Batteries II. Structure, Composition, and Properties. *J. Electrochem. Soc.* **2000**, *147* (7), 2478. https://doi.org/10.1149/1.1393556.

(25) Leriche, J. B.; Hamelet, S.; Shu, J.; Morcrette, M.; Masquelier, C.; Ouvrard, G.; Zerrouki, M.; Soudan, P.; Belin, S.; Elkaïm, E.; Baudelet, F. An Electrochemical Cell for Operando Study of Lithium Batteries Using Synchrotron Radiation. *J. Electrochem. Soc.* **2010**, *157* (5), A606. https://doi.org/10.1149/1.3355977.

(26) Landrot, G. 2018. FASTOSH: a software to process XAFS data for geochemical & environmental applications. In: Golschmidt Abstracts. Boston. pp. 1402.

(27) Shannon, R. D. Revised Effective Ionic Radii and Systematic Studies of Interatomic Distances in Halides and Chalcogenides. *Acta Cryst A* **1976**, *32* (5), 751–767. https://doi.org/10.1107/S0567739476001551.

(28) Yabuuchi, N.; Hara, R.; Kajiyama, M.; Kubota, K.; Ishigaki, T.; Hoshikawa, A.; Komaba, S. New O2/P2-Type Li-Excess Layered Manganese Oxides as Promising Multi-

Functional Electrode Materials for Rechargeable Li/Na Batteries. *Adv. Energy Mater.* **2014**, *4* (13), 1301453. https://doi.org/10.1002/aenm.201301453.

(29) Balsys, R. J.; Lindsay Davis, R. The Structure of $Li_{0.43}Na_{0.36}CoO_{1.96}$ Using Neutron Powder Diffraction. *Solid State Ion.* **1994**, *69* (1), 69–74. https://doi.org/10.1016/0167-2738(94)90451-0.

(30) Berthelot, R.; Pollet, M.; Carlier, D.; Delmas, C. Reinvestigation of the OP4-(Li/Na)CoO_2 -Layered System and First Evidence of the (Li/Na/Na)CoO_2 Phase with OPP9 Oxygen Stacking. *Inorg. Chem.* **2011**, *50* (6), 2420–2430. https://doi.org/10.1021/ic102218w.

(31) Casas-Cabanas, M.; Reynaud, M.; Rikarte, J.; Horbach, P.; Rodríguez-Carvajal, J. *FAULTS*: A Program for Refinement of Structures with Extended Defects. *J. Appl. Crystallogr.* **2016**, *49* (6), 2259–2269. https://doi.org/10.1107/S1600576716014473.

(32) Kawai, K.; Shi, X.-M.; Takenaka, N.; Jang, J.; Mortemard de Boisse, B.; Tsuchimoto, A.; Asakura, D.; Kikkawa, J.; Nakayama, M.; Okubo, M.; Yamada, A. Kinetic Square Scheme in Oxygen-Redox Battery Electrodes. *Energy Environ. Sci.* **2022**, *15*, 2591-2600. https://doi.org/10.1039/d1ee03503g.

(33) Seguin, L.; Amatucci, G.; Anne, M.; Chabre, Y.; Strobel, P.; Tarascon, J. M.; Vaughan, G. Structural Study of NiO_2 and CoO_2 as End Members of the Lithiated Compounds by in Situ High Resolution X-Ray Powder Diffraction. *J. Power Sources* **1999**, *81–82*, 604–606. https://doi.org/10.1016/S0378-7753(99)00110-X.

(34) Amatucci, G. G.; Tarascon, J. M.; Klein, L. C. CoO_2, The End Member of the Li_xCoO_2 Solid Solution. *J. Electrochem. Soc.* **1996**, *143* (3), 1114–1123. https://doi.org/10.1149/1.1836594.

(35) Carlier, D.; Saadoune, I.; Ménétrier, M.; Delmas, C. Lithium Electrochemical Deintercalation from O2-$LiCoO_2$. *J. Electrochem. Soc.* **2002**, *149* (10), A1310. https://doi.org/10.1149/1.1503075.

(36) Hy, S.; Cheng, J.-H.; Liu, J.-Y.; Pan, C.-J.; Rick, J.; Lee, J.-F.; Chen, J.-M.; Hwang, B. J. Understanding the Role of Ni in Stabilizing the Lithium-Rich High-Capacity Cathode Material $Li[Ni_xLi_{(1-2x)/3}Mn_{(2-x)/3}]O_2$ ($0 \leq x \leq 0.5$). *Chem. Mater.* **2014**, *26* (24), 6919–6927. https://doi.org/10.1021/cm501664y.

(37) Dixon, D.; Mangold, S.; Knapp, M.; Ehrenberg, H.; Bhaskar, A. Direct Observation of Reductive Coupling Mechanism between Oxygen and Iron/Nickel in Cobalt-Free Li-Rich Cathode Material: An in Operando X-Ray Absorption Spectroscopy Study. *Adv. Energy Mater.* **2021**, *11* (24), 2100479. https://doi.org/10.1002/aenm.202100479.

For Table of Contents Only